First Electrodeposition of Silicon on Crumbled MXene (c-Ti$_3$C$_2$T$_x$) for High-Performance Lithium-Ion Battery Negative Electrode

Rehman Butt,[a, b, c] Aleena Gigi,[a, b] François Rabuel,[a, c] Mathieu Morcrette,*[a, c] and Jeremy Mallet*[b]

The demand for high energy density Li-ion batteries requires electrode materials with high capacity and long cycling stability. Silicon is among the most promising negative electrode materials due to its high theoretical capacity, abundant resources, and low working potential. However, its poor conductivity and significant volume expansion during cycling limit its practical application. To overcome these issues, this study develops a two-step synthesis method for a nanostructured composite based on silicon as the active material. First, a crumbled Ti$_3$C$_2$T$_x$ (c-Ti$_3$C$_2$T$_x$) structure formed through electrostatic interaction between a Ti$_3$C$_2$T$_x$ suspension and 1 M KOH. Then, an amorphous silicon layer is electrodeposited onto the c-Ti$_3$C$_2$T$_x$ flakes in a room-temperature ionic liquid, creating the Si/c-Ti$_3$C$_2$T$_x$ composite for the negative electrode of Li-ion batteries. The c-Ti$_3$C$_2$T$_x$ structure enhances conductivity, provides mechanical stability to accommodate silicon's expansion, and offers nanostructured porosity for lithium-ion diffusion. The composite material demonstrates exceptional cycling stability, achieving a capacity of 1300 mAh g^{-1} at C/5 with 91% capacity retention after 100 cycles.

Introduction

Lithium-ion batteries (LIBs) are a type of rechargeable battery, and owing to their high energy density and low self-discharge, they are commonly used in portable electronics, electric vehicles, and other applications.[1–3] The graphite negative electrode of the LIB is undesirable because of its low capacity of 372 mAh g^{-1}.[4–6] Si anodes are promising candidates for achieving better capacity, with their high theoretical capacity of 3579 mAh g^{-1}, corresponding to the formation of the ending lithiation product Li$_{15}$Si$_4$.[7,8] Nevertheless, Si-based anodes have low electronic conductivity (10^{-3} S m^{-1} at RT) and suffer from massive volume expansion (approximately 270%) during lithiation/de-lithiation.[9–12] Ma-

terials with low conductivity slow down electron movement, which in turn hinders ion diffusion in the electrode during battery cycling. Moreover, silicon volume expansion creates cracks in the electrode material, which leads to the active material's detachment from the current collector and deterioration of the battery performance within a few cycles.[13]

To commercialize and improve the performance of the Si negative electrodes, it is crucial to tackle the Si volume expansion and increase the cyclic stability. Many structures of Si have been studied, such as SiO$_x$,[14] micro silicon,[15] Siloxene,[16] Silicon-metal alloys,[17,18] silicon nanowires, nanosheets, and nanospheres to control the volume expansion.[19–23] Furthermore, to overcome the conductivity problem, the Si anodes have been combined with many carbon-based materials.[22,24] One pathway is the layer-by-layer technique for trapping silicon nanoparticles between graphene sheets, which improved the conductivity, but the unstable lamellar structure could not control the silicon volume expansion.[25–27]

Another two-dimensional material, titanium carbide (Ti$_3$C$_2$T$_x$), has been attracting researchers' attention since its discovery in 2011 by Prof. Yury Gogotsi and Michel W. Barsoum due to its extraordinary physiochemical properties.[29–31] Ti$_3$C$_2$T$_x$ have high conductivity 4600 S cm^{-1} and Li$^+$ ion diffusion (10^{-10}–10^{-9} cm^2 s^{-1}).[32] Moreover, the surface of the MXene sheets is loaded with surface terminations that can provide attachment points for different groups.[33–36] Kong et al. prepared a Si/Ti$_3$C$_2$T$_x$ composite by mixing Si nanoparticles with MXene under ultrasonication, and when used as a negative electrode for LIB, it showed a reversible capacity of 188 mAh g^{-1} after 100 cycles at 200 mA g^{-1}.[32] However, in such structuration, the electrical contact between the silicon and the MXene flakes is not

[a] R. Butt, A. Gigi, F. Rabuel, M. Morcrette
Laboratoire de Réactivité et Chimie des Solides, LRCS, CNRS UMR 7314, Université de Picardie Jules Verne, 33 Rue Saint-Leu, 80039 Amiens Cedex, France
E-mail: jeremy.mallet@univ-reims.fr

[b] R. Butt, A. Gigi, J. Mallet
Laboratoire Lumière, nanomatériaux, nanotechnologies, L2n, Université de Technologies de Troyes, CNRS UMR 7076, Université de Reims Champagne-Ardenne, Campus du moulin de la Housse, 51685 Reims Cedex2, France
E-mail: mathieu.morcrette@u-picardie.fr

[c] R. Butt, F. Rabuel, M. Morcrette
Reseau sur le Stockage Electrochimique de l'Energie (RS2E), CNRS FR3459, 33 Rue Saint Leu, 80039 Amiens Cedex, France

📄 Supporting information for this article is available on the WWW under https://doi.org/10.1002/batt.202400633

optimized, and the electrons have to percolate through flakes to find silicon nanoparticles or spheres.

Herein, we report a conformal electrodeposition of amorphous silicon on crumbled-$Ti_3C_2T_x$ (c-$Ti_3C_2T_x$) sheets using a room-temperature ionic liquid (RTIL) to form a Si/c-$Ti_3C_2T_x$ composite. Crumbled-$Ti_3C_2T_x$ (c-$Ti_3C_2T_x$) provided high conductivity and strength to the composite structure. The open spaces in the c-$Ti_3C_2T_x$ structure accommodated the Si expansion during the charge/discharge cycles and prevented the electrode from cracking.

Results and Discussion
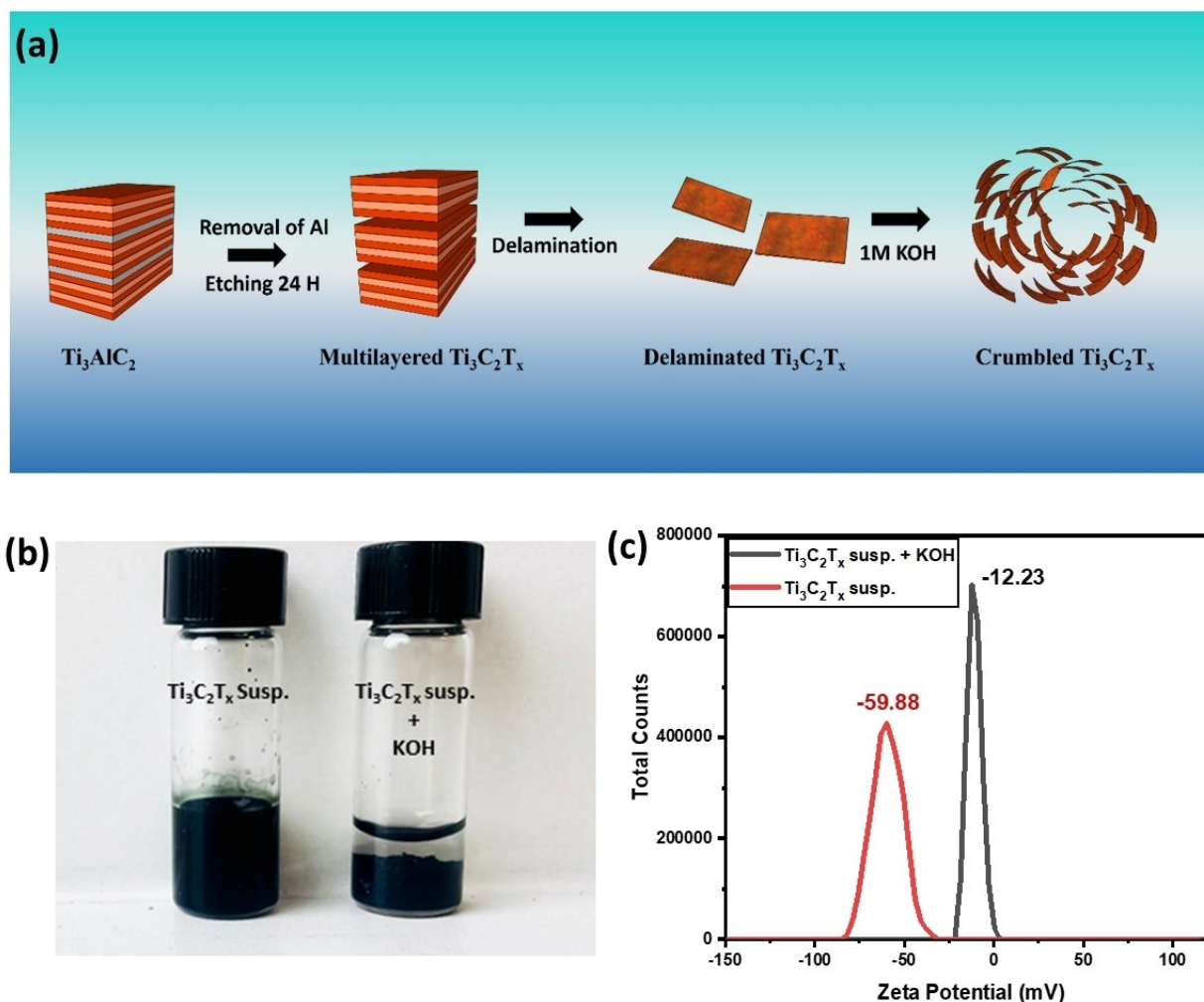
Synthesis of Crumbled $Ti_3C_2T_x$ (c-$Ti_3C_2T_x$)

$Ti_3C_2T_x$ flakes are obtained through a selective etching of the ternary compound precursor Ti_3AlC_2 (provided by A.J. Drexel Nanomaterials Institute). To etch the Al layer from the Ti_3AlC_2 (average particle size 32 μm), a mixture of HF, HCl, and deionized water was prepared in a ratio of 1:6:3. Ti_3AlC_2 was

added under constant stirring at 35 °C and kept under stirring for 24 hours. Next, the suspension was centrifuged and washed with deionized water until the pH reached 6–7. For the delamination, LiCl was added to the prepared $Ti_3C_2T_x$ powder and maintained under constant stirring for 18 hours at room temperature. Subsequently, the mixture was washed at least five times before collecting $Ti_3C_2T_x$ flakes.[37]

Colloidal suspension of $Ti_3C_2T_x$ sheets was mixed with a 1 M solution of KOH at room temperature, resulting in immediate flocculation of the sheets.[38] The resulting material was separated from the solution through centrifugation and washed with water and ethanol until neutral. The materials obtained were finally freeze-dried for 24 hours to retain the crumbled structuration (c-$Ti_3C_2T_x$). Figure 1a shows the pictorial representation of the synthesis of crumbled $Ti_3C_2T_x$ (c-$Ti_3C_2T_x$). The addition of KOH to $Ti_3C_2T_x$ colloidal suspension modifies the zeta potential due to the interaction between the negative surface termination of $Ti_3C_2T_x$ sheets and K$^+$ ions.[38,39] As soon as delaminated $Ti_3C_2T_x$ suspension interacts with the K$^+$ ions, it settles down quickly, forming agglomerates (Figure 1b), and Zeta potential (Zetasizer Nano

Figure 1. (a) Systematic diagram illustrating the step-by-step synthesis of Crumbled $Ti_3C_2T_x$ (c- $Ti_3C_2T_x$) (b) Digital photograph of delaminated $Ti_3C_2T_x$ suspension with and without KOH. (c) Zeta Potential of delaminated $Ti_3C_2T_x$ suspension with and without KOH.

Batteries & Supercaps

Research Article
doi.org/10.1002/batt.202400633

Chemistry Europe
European Chemical
Societies Publishing

ZS) shifts from -59.88 mV due to the presence of negative surface terminations to -12.23 mV (Figure 1c). The decrease in zeta potential comes from the interaction between the negative surface termination of $Ti_3C_2T_x$ and the K^+ ions.

To compare the impact of $c-Ti_3C_2T_x$ porosity on the Si electrodeposition, we prepared a free-standing $Ti_3C_2T_x$ film using vacuum filtrating $Ti_3C_2T_x$ suspension for 12 hours on the Whatman filter paper. Water residue was removed by drying in the oven for 2 hours at $100\,°C$. The resultant film was highly stacked ($s-Ti_3C_2T_x$) and was used as such for the electrodeposition experiments.

### Characterization of Crumbled $Ti_3C_2T_x$ ($c-Ti_3C_2T_x$)

MAX precursor and MXene have been characterized by X-ray diffraction (D4 Endeavor diffractometer using Cu Kα radiation). XRD pattern of Ti_3AlC_2 showed its signature peak (104) at $39°$, and it vanished after the etching of the Al layer from the complex (Figure 2a). The peak at $9.5°$ (002) for Ti_3AlC_2 shifted to a lower angle of $6.3°$ for $c-Ti_3C_2T_x$ after the removal of the aluminum layer and delamination of the multilayered powder by LiCl. The shift indicated that the distance between the layers had increased after the removal of the Al layers

and delamination of $c-Ti_3C_2T_x$. The chemical composition of the Ti_3AlC_2 and $c-Ti_3C_2T_x$ was analyzed by the Energy Dispersive X-ray (EDX) spectroscopy by mapping their top surface (Figure 2b). Ti_3AlC_2 showed prominent peaks for the Ti, Al, and C. After etching and delamination, the Al peak disappeared for $c-Ti_3C_2T_x$, and peaks emerged for the surface terminations (F, O, and Cl). Moreover, a small peak also appeared for the residue K^+ ions trapped between the layers.[38] Figure 2c shows the SEM (JEOL, JSM-7900F) image of the $c-Ti_3C_2T_x$ freeze-dried powder. A crumbled structure with many open spaces can be seen when compared to free-standing vacuum-dried films that are highly stacked ($s-Ti_3C_2T_x$) and don't have any pathway for the electrolyte to navigate inside the structure (Figure S1). However, in the case of the $c-Ti_3C_2T_x$ structure, large open spaces of up to a few microns were retained when this powder was used to make electrodes on stainless-steel foil through slurry (Figure 2d).

Synthesis of Si/$c-Ti_3C_2T_x$ Composite

Before Si electrodeposition, dried crumbled-$Ti_3C_2T_x$ ($c-Ti_3C_2T_x$) powder was mixed with polyvinylidene fluoride (PVDF) in a
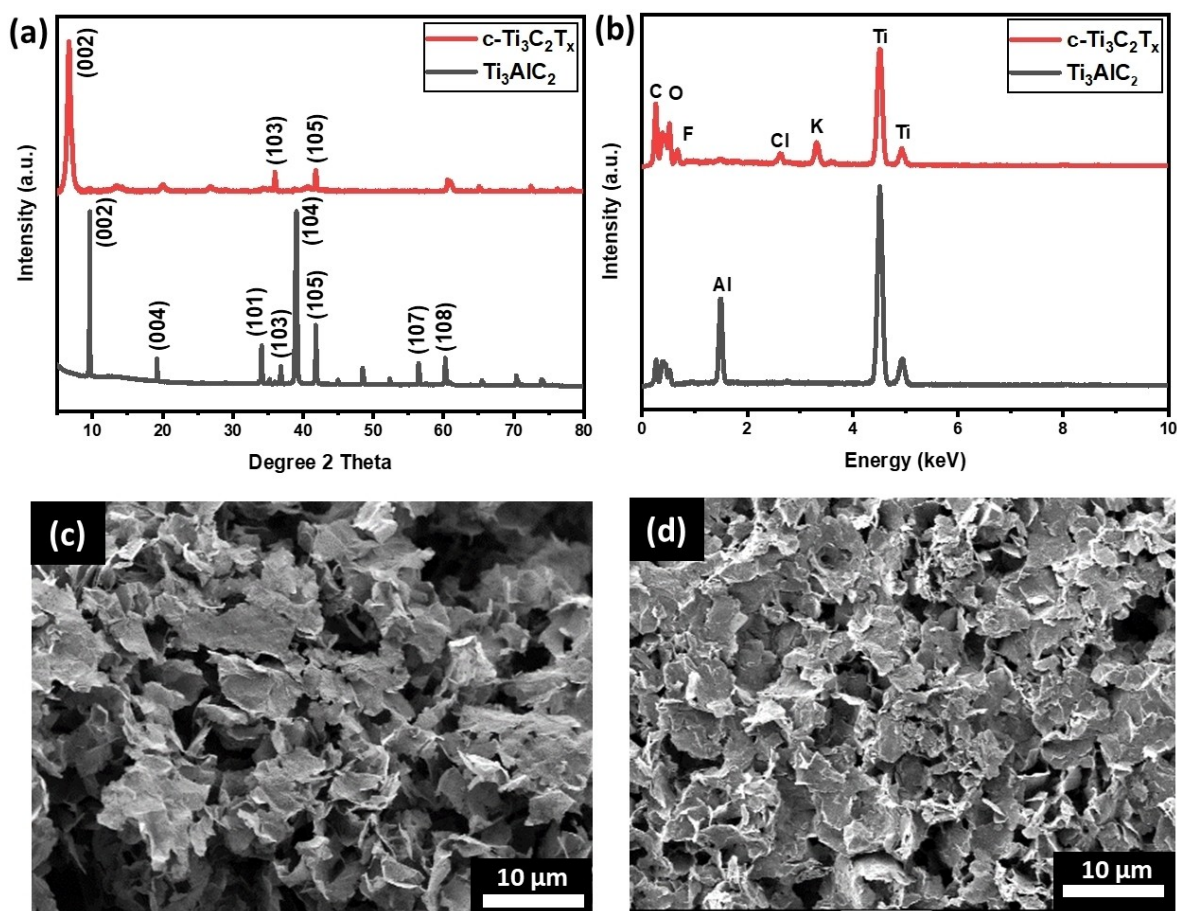
Figure 2. (a) XRD pattern of Ti_3AlC_2, $c-Ti_3C_2T_x$ powder. (b) EDX pattern of Ti_3AlC_2 and $c-Ti_3C_2T_x$. SEM Images of (c) $c-Ti_3C_2T_x$ powder and (d) $c-Ti_3C_2T_x$ slurry on Stainless steel foil.

90:10 weight ratio in a mortar and pestle. N-methyl-2-pyrrolidone (NMP) was used as the solvent to make a homogeneous slurry and stirred for 18 h at room temperature. The resulting slurry was uniformly tape cast using a doctor blade on a stainless steel foil and dried at 60 °C for 12 h and then at 120 °C for another 12 h in a vacuum oven to remove any NMP and water content. The final slurry used as a substrate for the electrodeposition.

Silicon was electrodeposited on c-$Ti_3C_2T_x$ electrodes using Volta lab (PGZ 100 & 301) in an electrolyte consisting of 1-butyl-1-methylpyrrolidinium bis(trifluoromethanesulfonyl)imide (Py$_{1,4}$[TFSI]) (Solvionic, 99.9 %) and 0.1 M SiCl$_4$ (Aldrich, 99.99 %) at room temperature.[40] Before electrodeposition, the ionic liquid underwent drying for 72 hours at 100 °C under a vacuum inside a glove box. Electrochemical studies were performed in an argon-filled glove box with H_2O and O_2 content of less than one ppm. The electrodeposition was carried out in potentiostatic mode using c-$Ti_3C_2T_x$ as the working electrode, platinum wires as the counter electrode, and quasi-reference electrode (QRE). The reference and counter electrodes were cleaned by sonication in acetone, ethanol, and deionized water. Finally, the electrodes were dried with hydrogen flame to remove residual impurities before the cell setup. Si/c-$Ti_3C_2T_x$ composite electrodes were synthesized by electrodepositing Si at a potential of -2.5 V *vs.* Pt at 100 °C. The silicon content in the composite has been adjusted by controlling the electrochemical charge to 2 Coulombs, corresponding to 0.145 mg of Si. The calculated mass is, however, overestimated as the Faradaic efficiency is not 100 % because a low percentage of the observed current is reducing the ionic liquid species and possibly participating in substrate reconstruction.[41] After electrodeposition, the composite electrodes underwent immediate cleaning with dimethyl carbonate (DMC) solvent inside the glove box.

Figure 3a shows the cell setup used for the silicon electrodeposition. The cyclic voltammetry was carried out on c-$Ti_3C_2T_x$ electrodes in pure Py$_{1,4}$(TFSI) and 0.1 M SiCl$_4$ in Py$_{1,4}$(TFSI) ionic liquid electrolyte with 10 mV s^{-1} scan rate at 100 °C (Figure 3b). In the case of pure Py$_{1,4}$(TFSI), no significant current was observed up to -3 V *vs.* Pt, confirming no interaction between the substrate and the ionic liquid. It also shows a stable electrochemical window of approximately 4.7 V *vs.* Pt, with degradation starting after -2.7 V *vs.* Pt. The pure ionic liquid was also tested under the same conditions on the Au substrate, and it showed minimal current when compared to the c-$Ti_3C_2T_x$ substrate (Figure S2). The slight current increase in the case of c-$Ti_3C_2T_x$ could correspond to the trapped water molecules inside the c-$Ti_3C_2T_x$ layers. Cyclic Voltammetry of 0.1 M SiCl$_4$ in Py$_{1,4}$(TFSI) electrolyte on c-$Ti_3C_2T_x$ substrate shows a significant increase in cathodic current starting at -2.2 V *vs.* Pt, followed by the diffusion plateau corresponding to the Si deposition on c-$Ti_3C_2T_x$ flakes.[41] While on the reverse scan, no anodic peak was observed in the potential range, confirming the irreversibility of the freshly deposited silicon.[40,42]

Figure 3c shows the potentiostatic curves of the silicon deposition on the stacked $Ti_3C_2T_x$ and c-$Ti_3C_2T_x$ electrodes at -2.5 V *vs.* Pt in 0.1 M SiCl$_4$ in Py$_{1,4}$(TFSI). Firstly, silicon deposition was done on stacked $Ti_3C_2T_x$ at 50 °C, and a very low current was observed because of the lack of available surface area for the silicon deposition, and only 0.2 Coulombs charge was transferred in 20 mins. The observed current and amount of charge increased for the c-$Ti_3C_2T_x$ substrate under the same conditions correspond to the increased silicon deposition because of the availability of more active surface area. The highest current and charge were observed for the c-$Ti_3C_2T_x$ substrate at 100 °C because the increased temperature lowers the viscosity of the electrolyte, which, in turn, increases the access of silicon ions inside the electrode, favoring deposition. In all the cases, the current decreases sharply at the start as the species at the electrode-electrolyte interface deplete quickly. After that, the silicon nucleation forms highly active silicon nuclei that act as sites or clusters where additional silicon atoms can attach, favoring electrodeposition.[43] Then, the current slowly decreases as the silicon deposits decrease the conductivity and the active available surface area for further Si deposition.

Characterization of Si/c-$Ti_3C_2T_x$ Composite

XRD pattern for Si/c-$Ti_3C_2T_x$ composite retained the (002) peak corresponding to c-$Ti_3C_2T_x$. Still, the peak shifted to a lower angle (6°), referring to increased interlayer spacing (Figure 4a). The increased interlayer distance could be attributed to the intercalation of Si^{+4} and Py$_{1,4}^+$ ions within the c-$Ti_3C_2T_x$ layers during the electrodeposition process.[44] Figure 4b shows the SEM image of the top surface of the Si/c-$Ti_3C_2T_x$ composite after 2 Coulombs (0.145 mg) silicon electrodeposition at 100 °C. A thick and uniform silicon layer is visible on the surface, filling all the pores within the structure. On the cross-section SEM image of the composite, thick silicon deposits can be observed on the c-$Ti_3C_2T_x$ flakes, confirming the penetration of the electrolyte inside the pores of the c-$Ti_3C_2T_x$ substrate (Figure 4c–d). Cross-sectional images further revealed that the silicon layer thickness on the flakes decreases steadily toward the bottom of the electrode. This decrease can be attributed to the reduced availability of pathways for electrolyte diffusion at the surface, caused by the newly deposited silicon layer. However, such homogenous and in-depth silicon layer deposition in the electrode could be impossible to achieve through physical vapor deposition (PVD) or chemical vapor deposition (CVD).[45]

The chemical composition of the c-$Ti_3C_2T_x$ and Si/c-$Ti_3C_2T_x$ was analyzed by the Energy Dispersive X-ray (EDX) spectroscopy by mapping their top surfaces (Figure 4e). The c-$Ti_3C_2T_x$ showed prominent peaks for the Ti and C. After silicon deposition, the intensity of the Ti and C peaks decreases, and a sharp peak appears for the silicon, confirming the presence of Si deposits on the flakes. EDX studies were also conducted to compare the silicon content on the surface and inside the electrode after 20 minutes of deposition on the s-$Ti_3C_2T_x$ and
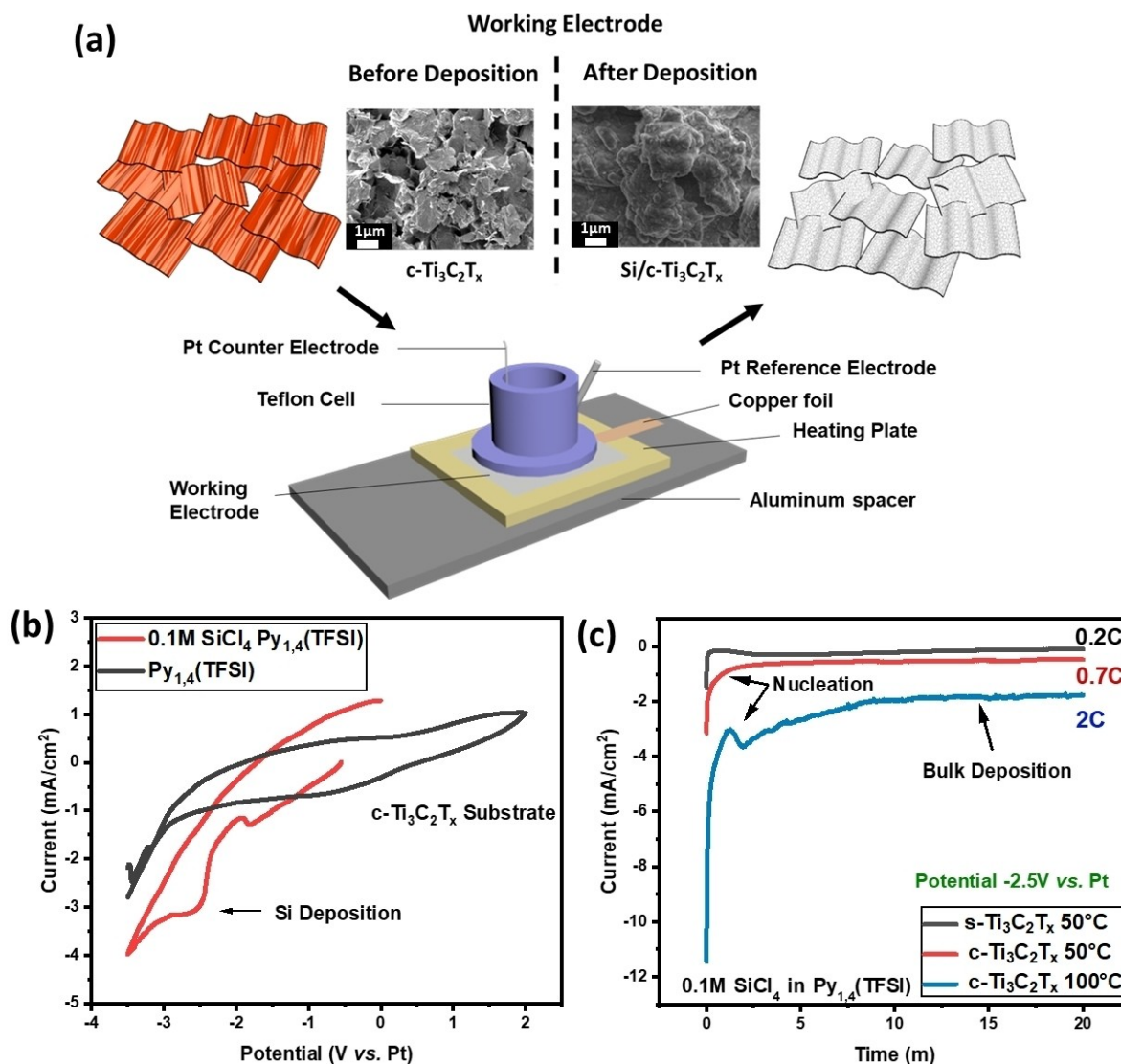
Figure 3. (a) Silicon Electrodeposition setup in a homemade Teflon cell. (b) CV of pure $Py_{1,4}$(TFSI) and 0.1 M $SiCl_4$ in $Py_{1,4}$(TFSI) ionic liquid on c-$Ti_3C_2T_x$ electrodes vs. Pt at 10 mV s^{-1} (c) Chronoamperometry at -2.5 V vs. Pt on s-$Ti_3C_2T_x$ film at 50 °C, and on c-$Ti_3C_2T_x$ electrodes at 50 °C and 100 °C.

c-$Ti_3C_2T_x$ substrates at different temperatures (Figure S3). For s-$Ti_3C_2T_x$, silicon was only electrodeposited on the surface, and no silicon was detected between s-$Ti_3C_2T_x$ layers due to the very dense stacking of the sheets. On the other hand, the c-$Ti_3C_2T_x$ substrate exhibited much better wettability by the electrolyte, allowing more homogeneous silicon deposition inside the electrodes and confirming the advantage of utilizing crumbled structuration. When the temperature increased from 50 °C to 100 °C, the silicon content inside the electrode increased exponentially. This increase is attributed to reduced viscosity and increased diffusion of silicon species in the substrate at higher temperatures.[41]

Raman spectroscopy (Horiba LabRAM HR Evolution with 785 nm) has been done on the c-$Ti_3C_2T_x$ and Si/c-$Ti_3C_2T_x$ composite to study the c-$Ti_3C_2T_x$ structure, surface termination and to confirm silicon deposition on the $Ti_3C_2T_x$ flakes (Figure 4f). For c-$Ti_3C_2T_x$, the peak at 204 cm^{-1} is the most intense, consisting of E_g and A_{1g} modes. These modes

correspond to in-plane and out-plane vibrations of the surface titanium atoms, carbon, and surface termination as a group.[46] The peaks at 286, 390, and 619 cm^{-1} correspond to E_g in-plane vibration of the $(OH)_2$ surface terminations attached to Ti atoms formed due to the aqueous synthesis process of c-$Ti_3C_2T_x$.[46] A peak at 574 cm^{-1} corresponds to the A_{1g} mode, an out-plane vibration of the O_2 surface termination attached to the surface Ti atoms.[47] The peak at 724 cm^{-1} originates from the A_{1g} and E_g modes, which are the out-of-plane and in-plane vibrations of the C atoms in the c-$Ti_3C_2T_x$ structure.[46] Raman spectra of Si/c-$Ti_3C_2T_x$ showed only a single broad peak at 510 cm^{-1}, corresponding to silicon deposition on the c-$Ti_3C_2T_x$ flakes. No signal was observed for c-$Ti_3C_2T_x$ because the silicon deposits cover the c-$Ti_3C_2T_x$ flakes homogenously.[48]
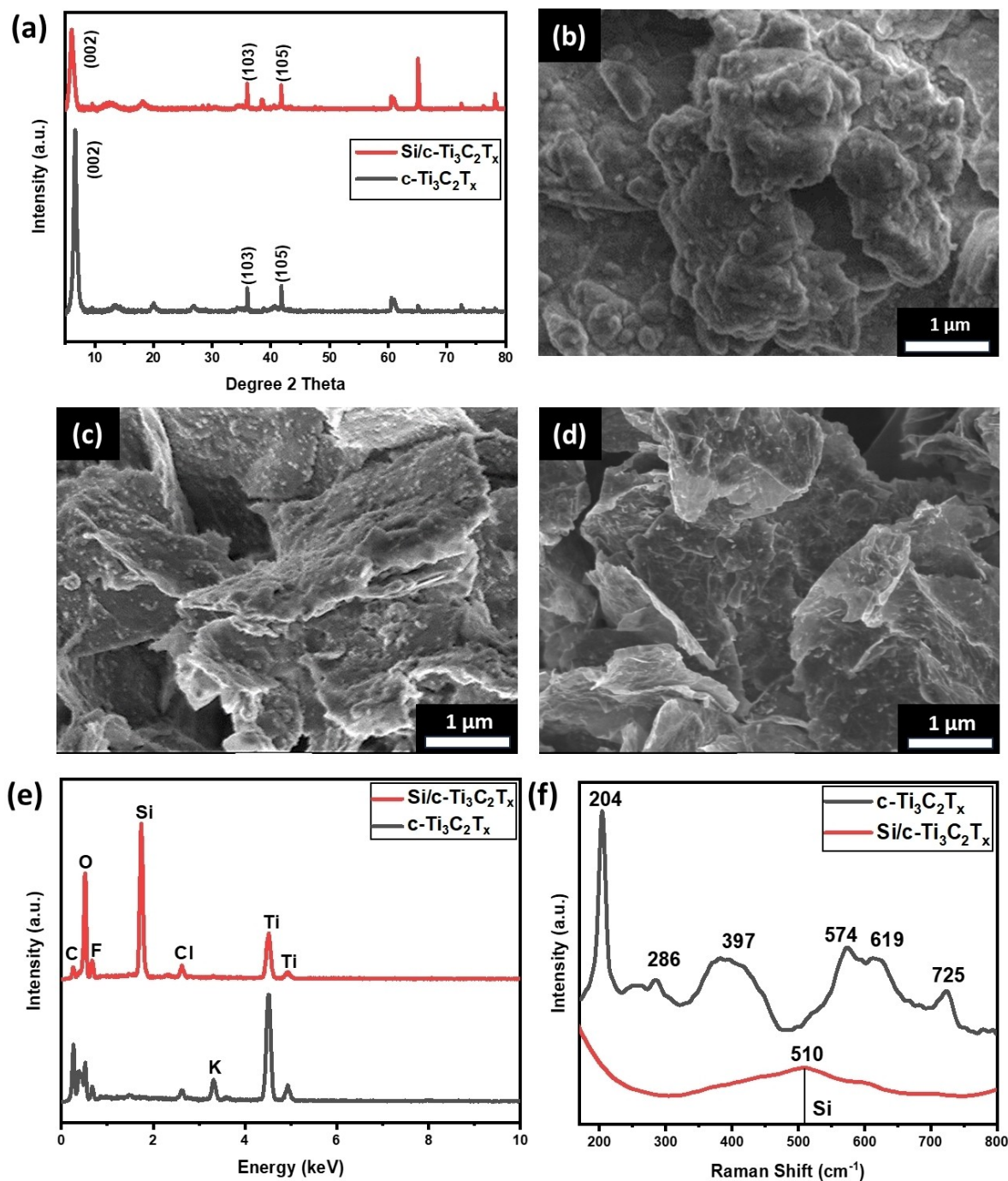
Figure 4. (a) XRD pattern of c-Ti$_3$C$_2$T$_x$ powder and Si/c-Ti$_3$C$_2$T$_x$ composite. SEM image after Si deposition on the c-Ti$_3$C$_2$T$_x$ electrode (b) Top surface, (c) Cross-section close to the surface, (d) close to the bottom of electrode. (e) EDX pattern of c-Ti$_3$C$_2$T$_x$ and Si/c-Ti$_3$C$_2$T$_x$ composite. (f) Raman Spectrum of c-Ti$_3$C$_2$T$_x$ and Si/c-Ti$_3$C$_2$T$_x$ composite.

Electrochemical Performance of c-Ti$_3$C$_2$T$_x$ and Si/c-Ti$_3$C$_2$T$_x$ Composites as Negative Electrode for Li-Ion Batteries

To investigate the silicon stability in the Si/c-Ti$_3$C$_2$T$_x$ composite, it was used as a negative electrode for Li-ion batteries in half coin-cell (CR2032). The coin cells were assembled in an argon-filled glove box, utilizing the Si/c-Ti$_3$C$_2$T$_x$ composite as a working electrode, lithium foil was employed as a counter/reference electrode, 1 M LiPF$_6$ in ethylene carbonate/dimeth-yl (EC/DMC, 1:1 V/V) with 10% fluoroethylene carbonate (FEC) served as an electrolyte, and glass fiber was used as a separator. FEC aids stable SEI layer formation, which leads to better capacity retention during battery cycling.[48] For comparison, the c-Ti$_3$C$_2$T$_x$ electrode without Si deposition was also tested as a negative electrode. Galvanostatic charge/discharge was performed in a potential range of 0.01–3 V vs. Li/Li$^+$ for both c-Ti$_3$C$_2$T$_x$ and Si/c-Ti$_3$C$_2$T$_x$ composite electrodes at C/5.

Electrodes with only 2 Coulombs (0.145 mg) silicon deposits at 100°C were chosen because of their ability to withstand battery preparation without cracking. Figure 5a shows the first cycle of the differential capacity plot of the pure c-$Ti_3C_2T_x$ and Si/c-$Ti_3C_2T_x$. For c-$Ti_3C_2T_x$, a broad peak between 1.25 V and 1.75 V vs. Li/Li$^+$ during charge and discharge shows lithiation and de-lithiation in the c-$Ti_3C_2T_x$ electrode.[49,50] Conversely, for the lithiation and de-lithiation in the Si/c-$Ti_3C_2T_x$, no peak was observed for the c-$Ti_3C_2T_x$. However, silicon lithiation was observed at 0.23 V vs. Li/Li$^+$, and a corresponding de-lithiation of the silicon was observed at 0.3 V vs. Li/Li$^+$.[40] This behaviour got more pronounced as the cycling progressed (Figure S4). The lithiation of the silicon can also be confirmed from the charge and discharge profile of the composite (Figure 5b). The plateau around 0.2 V vs. Li/Li$^+$ for Si/c-$Ti_3C_2T_x$ shows the lithiation of the deposited silicon. This behaviour explains Li$^+$ intercalation only in the silicon in the case of composite. The reason was the silicon deposits on the c-$Ti_3C_2T_x$ flakes blocked the access of the Li$^+$ to the surface terminations and underneath layers of c-$Ti_3C_2T_x$. Figure 5c shows the cyclic stability of c-$Ti_3C_2T_x$ and Si/c-$Ti_3C_2T_x$ composite at C/5 rate. c-$Ti_3C_2T_x$ showed a capacity of 70 mAh g^{-1}, and for composite, when considering Si/c-$Ti_3C_2T_x$ as active material, it showed a capacity of 85 mAh g^{-1} at C/5

after 100 cycles. For activation of silicon at the start, an additional three cycles were done at C/20 (Figure S5a). However, Li$^+$ intercalation was only possible for the silicon in the case of composite. Figure 5d shows the cyclic performance of the composite, considering only silicon as an active material (0.145 mg) in the composite, and it shows an astonishing capacity of 1300 mAh g^{-1} at C/5 with 91% capacity retention after 100 cycles. For the activation of silicon, at the start, an additional 3 cycles were carried out at C/20 (Figure S5b). The initial increase in specific capacity over the first 20 cycles can be attributed to the delayed activation of silicon, after which the capacity stabilized up to 100 cycles.[51–53] The minor fluctuations observed during the cycling are likely due to the temperature fluctuation of the cycling room, as they are also present for bare c-$Ti_3C_2T_x$ cycling (Figure S6). However, these fluctuations did not impact the specific capacity of silicon, which remained stable and demonstrated a high coulombic efficiency of 99.5%.

Conclusions

In this study, a nanostructured composite negative electrode using a two-step method was successfully synthesized,
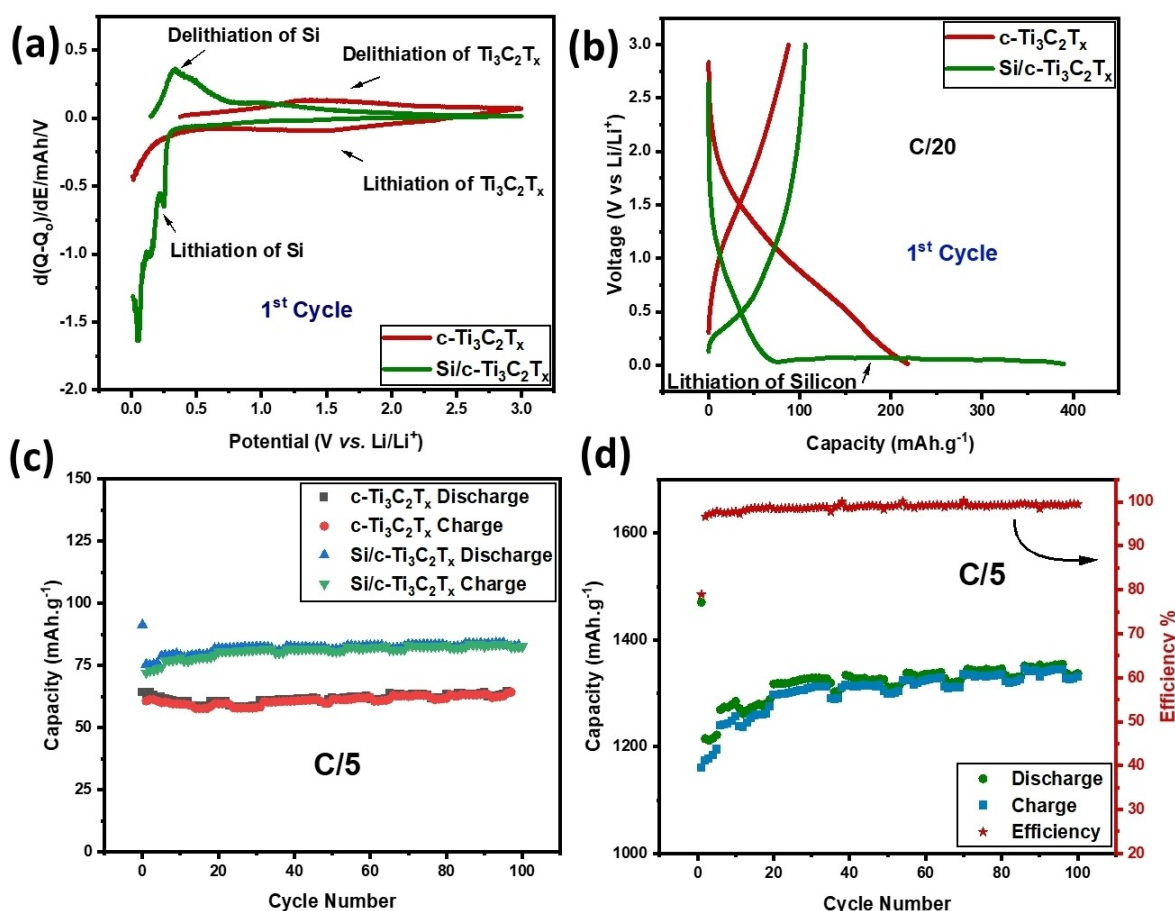
Figure 5. (a) Differential capacity plots of c-$Ti_3C_2T_x$ and Si/c-$Ti_3C_2T_x$ 1st cycle (b) Charge and discharge profile of c-$Ti_3C_2T_x$ and Si/c-$Ti_3C_2T_x$ at C/20 1st cycle. (c) Cyclic performance of c-$Ti_3C_2T_x$ and Si/c-$Ti_3C_2T_x$ at C/5 (d) Cyclic Performance of Si/c-$Ti_3C_2T_x$ when only Si is taken as active material. All experiments are cycled in the 3–0.01 V vs. Li/Li$^+$ voltage range in 1 M LiPF$_6$ EC/DMC (1:1 v/v) with 10% FEC electrolyte.

Batteries & Supercaps

Research Article
doi.org/10.1002/batt.202400633

Chemistry
Europe
European Chemical
Societies Publishing

demonstrating significant potential for improving the performance of high-energy density Li-ion batteries (LIBs). By crumbling $Ti_3C_2T_x$ sheets via electrostatic interaction with 1 M KOH and subsequently electrodepositing a conformal amorphous silicon layer in room-temperature ionic liquids, a Si/c-$Ti_3C_2T_x$ composite was developed. This innovative structuration not only enhanced the conductivity of the electrode but also effectively managed the volume expansion of silicon during cycling.

In the Si/c-$Ti_3C_2T_x$ composite, silicon exhibited outstanding cycling stability, with 1300 mAh g^{-1} capacity at C/5 with 91% capacity retention after 100 cycles as a negative electrode for LIBs. These results underscore the potential of the composite material to address the critical challenges associated with silicon-negative electrodes, namely poor conductivity, significant volume expansion, and cycling stability. This study highlights the importance of electrode structuration in enhancing the durability and performance of high-capacity materials, paving the way for developing next-generation Li-ion batteries with superior energy densities and long-term stability. Future work should optimize the composite structure, improve the silicon deposition inside the material, and explore its performance in full-cell configurations to realize its application potential in commercial LIBs.

Acknowledgements

Conflict of Interests

The authors declare no competing financial interest.

Data Availability Statement

The data that support the findings of this study are available from the corresponding author upon reasonable request.

[1] R. F. Service **2019**.
[2] G. Zubi, R. Dufo-López, M. Carvalho, G. Pasaoglu, *Renew. Sustain. Energy Rev.* **2018**, *89*, 292.
[3] X. Li, X. Zhu, A. Feng, M. An, P. Liu, Y. Zu, *J. Mater. Res. Technol.* **2024**, *29*, 5667.
[4] Y.-K. Sun, *ACS Energy Lett.* **2017**, *2*.
[5] Y. Li, Y. Lu, P. Adelhelm, M.-M. Titirici, Y.-S. Hu, *Chem. Soc. Rev.* **2019**, *48*, 4655.
[6] R. Jia, R. Zhang, L. Yu, X. Kong, S. Bao, M. Tu, X. Liu, B. Xu, *J. Colloid Interface Sci.* **2023**, *630*, 86.
[7] P. Li, G. Zhao, X. Zheng, X. Xu, C. Yao, W. Sun, S. X. Dou, *Energy Storage Mater.* **2018**, *15*, 422.
[8] X. Zuo, J. Zhu, P. Müller-Buschbaum, Y.-J. Cheng, *Nano Energy* **2017**, *31*, 113.
[9] S. Chae, M. Ko, K. Kim, K. Ahn, J. Cho, *Joule* **2017**, *1*, 47.
[10] Z. Karkar, T. Jaouhari, A. Tranchot, D. Mazouzi, D. Guyomard, B. Lestriez, L. Roué, *J. Power Sources* **2017**, *371*, 136.
[11] I. Yoon, D. P. Abraham, B. L. Lucht, A. F. Bower, P. R. Guduru, *Adv. Energy Mater.* **2016**, *6*, 1600099.
[12] J. Wang, H. Luo, Y. Liu, Y. He, F. Fan, Z. Zhang, S. X. Mao, C. Wang, T. Zhu, *Nano Lett.* **2016**, *16*, 5815.
[13] W.-F. Ren, Y. Zhou, J.-T. Li, L. Huang, S.-G. Sun, *Curr. Opin. Electrochem.* **2019**, *18*, 46.
[14] T. Chen, J. Wu, Q. Zhang, X. Su, *J. Power Sources* **2017**, *363*, 126.
[15] Q. Ma, Z. Zhao, Y. Zhao, H. Xie, P. Xing, D. Wang, H. Yin, *Energy Storage Mater.* **2021**, *34*, 768.
[16] L. C. Loaiza, L. Monconduit, V. Seznec, *J. Power Sources* **2019**, *417*, 99.
[17] Z. Du, J. Li, C. Daniel, D. Wood III, *Electrochim. Acta* **2017**, *254*, 123.
[18] J. Sun, J. Li, B. Ban, J. Shi, Q. Wang, J. Chen, *Electrochim. Acta* **2020**, *345*, 136242.
[19] W. Wang, Z. Favors, R. Ionescu, R. Ye, H. H. Bay, M. Ozkan, C. S. Ozkan, *Sci. Rep.* **2015**, *5*, 8781.
[20] C. K. Chan, R. N. Patel, M. J. O'Connell, B. A. Korgel, Y. Cui, *ACS Nano* **2010**, *4*, 1443.
[21] J. Tang, Q. Yin, Q. Wang, Q. Li, H. Wang, Z. Xu, H. Yao, J. Yang, X. Zhou, J.-K. Kim, L. Zhou, *Nanoscale* **2019**, *11*, 10984.
[22] Y. Qi, G. Wang, S. Li, T. Liu, J. Qiu, H. Li, *Chem. Eng. J.* **2020**, *397*, 125380.
[23] T. Zhao, D. Lan, Z. Jia, Z. Gao, G. Wu, *Nano Res.* **2024**, 1.
[24] Y. An, Y. Tian, C. Liu, S. Xiong, J. Feng, Y. Qian, *ACS Nano* **2022**, *16*, 4560.
[25] X. Zhou, Y. Liu, C. Du, Y. Ren, R. Xiao, P. Zuo, G. Yin, Y. Ma, X. Cheng, Y. Gao, *ACS Appl. Mater. Interfaces* **2019**, *11*, 39970.
[26] H. Wu, L. Zheng, N. Du, B. Sun, J. Ma, Y. Jiang, J. Gong, H. Chen, L. Wang, *ACS Appl. Mater. Interfaces* **2021**, *13*, 22323.
[27] A. Jamaluddin, B. Umesh, F. Chen, J.-K. Chang, C.-Y. Su, *Nanoscale* **2020**, *12*, 9616.
[28] J. Han, X. Tang, S. Ge, Y. Shi, C. Zhang, F. Li, S. Bai, *J. Mater. Sci. Technol.* **2021**, *80*, 259.
[29] M. Naguib, M. Kurtoglu, V. Presser, J. Lu, J. Niu, M. Heon, L. Hultman, Y. Gogotsi, M. W. Barsoum, *Adv. Mater.* **2011**, *23*, 4248.
[30] M. Naguib, M. W. Barsoum, Y. Gogotsi, *Adv. Mater.* **2021**, *33*, 2103393.
[31] G. Ma, D. Lan, Y. Zhang, X. Sun, Z. Jia, G. Wu, G. Bu, P. Yin, *Small* **2024**, 2404449
[32] F. Kong, X. He, Q. Liu, X. Qi, D. Sun, Y. Zheng, R. Wang, Y. Bai, *Electrochem. Commun.* **2018**, *97*, 16.
[33] Y.-T. Liu, P. Zhang, N. Sun, B. Anasori, Q.-Z. Zhu, H. Liu, Y. Gogotsi, B. Xu, *Adv. Mater.* **2018**, *30*, 1707334.
[34] Y. Lian, D. Lan, X. Jiang, L. Wang, S. Yan, Q. Dong, Y. Jiang, J. Gu, Z. Gao, G. Wu, *J. Colloid Interface Sci.* **2024**, *676*, 217.
[35] X. Xie, H. Wang, H. Kimura, C. Ni, W. Du, G. Wu, *Int. J. Miner. Metall. Mater.* **2024**, *31*, 2274.
[36] A. Feng, L. Liu, P. Liu, Y. Zu, F. Han, X. Li, S. Ding, Y. Chen, *Mater. Today Energy* **2024**, 101626.
[37] C. E. Shuck, A. Sarycheva, M. Anayee, A. Levitt, Y. Zhu, S. Uzun, V. Balitskiy, V. Zahorodna, O. Gogotsi, Y. Gogotsi, in *MXenes*, Jenny Stanford Publishing **2023**, pp. 539–560.
[38] D. Zhao, M. Clites, G. Ying, S. Kota, J. Wang, V. Natu, X. Wang, E. Pomerantseva, M. Cao, M. W. Barsoum, *Chem. Commun.* **2018**, *54*, 4533.
[39] R. Butt, A. H. Siddique, S. W. Bokhari, S. Jiang, D. Lei, X. Zhou, Z. Liu, *Int. J. Energy Res.* **2019**, *43*, 4995.
[40] A. W. Nemaga, J. Mallet, J. Michel, C. Guery, M. Molinari, M. Morcrette, *J. Power Sources* **2018**, *393*, 43.

Batteries & Supercaps

Research Article
doi.org/10.1002/batt.202400633

Chemistry Europe
European Chemical
Societies Publishing

[41] S. Thomas, D. Kowalski, M. Molinari, J. Mallet, *Electrochim. Acta* **2018**, *265*, 166.

[42] C. A. Vlaic, S. Ivanov, R. Peipmann, A. Eisenhardt, M. Himmerlich, S. Krischok, A. Bund, *Electrochim. Acta* **2015**, *168*, 403.

[43] J. L. Gole, *ECS Trans.* **2020**, *98*, 107.

[44] N. Jäckel, B. Krüner, K. L. Van Aken, M. Alhabeb, B. Anasori, F. Kaasik, Y. Gogotsi, V. Presser, *ACS Appl. Mater. Interfaces* **2016**, *8*, 32089.

[45] J. Brumbarov, J. Kunze-Liebhäuser, *J. Power Sources* **2014**, *258*, 129.

[46] A. Sarycheva, Y. Gogotsi, *Chem. Mater.* **2020**, *32*, 3480.

[47] T. Hu, J. Wang, H. Zhang, Z. Li, M. Hu, X. Wang, *Phys. Chem. Chem. Phys.* **2015**, *17*, 9997.

[48] Q. Yang, Z. Wang, Y. Xia, G. Wu, C. Chen, J. Wang, P. Rao, A. Dong, *J. Colloid Interface Sci.* **2020**, *580*, 68.

[49] A. Saha, N. Shpigel, Rosy, N. Leifer, S. Taragin, T. Sharabani, H. Aviv, I. Perelshtein, G. D. Nessim, M. Noked, Y. Gogotsi, *Adv. Funct. Mater.* **2021**, *31*, 2106294.

[50] F. Kong, X. He, Q. Liu, X. Qi, Y. Zheng, R. Wang, Y. Bai, *Electrochim. Acta* **2018**, *265*, 140.

[51] X. Dong, C. Woo, S. Oh, Y. Kim, X. Zhang, K. H. Choi, J. Kang, H.-S. Bang, J. Jeon, H.-S. Oh, D. Kim, *ACS Appl. Energy Mater.* **2024**, *7*, 7478.

[52] F. Lepoivre, D. Larcher, J.-M. Tarascon, *J. Electrochem. Soc.* **2016**, *163*, A2791.

[53] E. Barcaro, V. Marangon, M. Mutarelli, J. Hassoun, *J. Power Sources* **2024**, *595*, 234059.